Exploring the Radio Sky

N V Karthik

KRITTIKA SUMMER PROJECTS 2023
Exploring the Radio Sky

N V Karthik

Birla Institute of Technology and Science, Pilani

Abstract

Radio astronomy has made significant contributions to physics and astronomy by revolutionizing our understanding of the universe. It is involved in the discovery of cosmic microwave background radiation, supporting the Big Bang theory, and it also confirmed Einstein's theory of general relativity through the study of pulsars. Radio astronomy has also played a vital role in mapping the distribution of galaxies, exploring active galactic nuclei, and developing interferometry techniques for enhanced resolution and gravitational wave astronomy. By penetrating dust clouds and observing non-optical phenomena, radio astronomy continues to expand our knowledge of the universe and contribute to our understanding of fundamental physical laws.

This project aims to not only understand the physics of radio astronomy but also the engineering and data sciences involved in it. The initial chapters of the report will serve as an introductory material to both Radio Astronomy and the its data analysis methods. Activities at the end of each chapter will serve as a ground of application the concepts acquired till that point of time.

As the chapters progress, more widely used procedures of data handling are brought into focus. And this is done in parallel while studying transient phenomena like FRBs, Pulsars, etc., These topics form a major portion of active astronomy research in today's world.

This report seeks to cover the majority of basic radio astronomy methods, both theoretical and practical, and to go into as much detail as possible about how they developed. Finally, all source code for data handling methods using python are uploaded to the GitHub repository **here** in form of Jupyter ipython notebooks. The tasks using CASA can be closely followed from the CASA official guidelines available at **CASA Guides website**

Contents

1. Introduction To Radio Astronomy

Studying celestial phenomena from various astronomical observations have been taking place since the dawn of our civilizations. But these observations have been limited to visible wavelengths for the most part until the 1900's. Study of Electricity and Magnetism helped discovery of other bands of EM Waves, and the possibility of making observations in that bands. These revealed new phenomena which was invisible to us before. Radio Astronomy involves observing the night sky in radio frequency bands, which lies in the window of 10 MHz to 300 GHz (or 1mm to 30m in terms of wavelength). One of the first radio sources to be observed were the from the center of Milky Way galaxy and later bright sources like Cygnus A, Cassiopeia A, Crab Nebula etc., were found. These along with 471 other bright sources were catalogued with advanced interferometers in the Third Cambridge Catalog of Radio Sources (3C), thus starting widespread radio observations of the sky. During the 1960s, radio astronomy yielded discoveries of quasars, pulsars, masers, many radio galaxies, and the cosmic microwave background, with the discoveries of pulsars and CMB yielding Nobel Prizes. The discovery of CMB also holds as a possible evidence of Big Bang Theory. Apart from these Radio bands also revealed the "Synchrotron radiation" caused by continuous emissions from bright radio source, in which relativistic electrons emit photons as they spiral around magnetic field lines.

1.1 Spectroscopy

A powerful tool for analyzing the detected radiation is to examine its spectrum. Spectrographs used at radio wavelengths are quite different. It is cumbersome to refract or diffract radio waves by optical means, so usually the separation of the different frequencies is accomplished electronically. The radio-frequency spectrum appears to the user as a graph of intensity or flux density (i.e., the amount of radiation) versus frequency or wavelength. All commonly observed spectra are

divided into 3 types

- Continuous spectra: When a radiation source emits at all frequencies over a range without breaks, the spectrum is called a continuous spectrum and the emitting object is called a continuum source.
- Bright line or emission line spectra: When a radiating object emits radiation only at some very specific frequencies, or wavelengths, the spectrum contains a set of discrete bright lines. These lines of light are called emission lines. They are characterized in the spectrum by 'peaks' appearing at discrete frequencies/wavelengths.
- Dark line or absorption line spectra: A more complicated and interesting case arises when the radiation from an intense continuum source passes through a cool, transparent gas of atoms or molecules. Some of the atoms or molecules in the gas can absorb photons from the continuum to raise them into a higher allowed energy level, thus forming 'dips' occurring at discrete frequencies/ wavelengths in the spectrum.

The atomic or molecular absorption frequencies are the same as the corresponding emission frequencies, and so again, the chemical composition of a gas cloud can be identified by the frequencies of the absorption lines that it produces.

1.2 Celestial Coordinates

Apart from the equipment to make observations, a robust way of pinpointing sources in the night sky is equally essential, to prepare and share astronomy catalogs. The following are some commonly used coordinates.

- Right Ascension and Declination

    1. RA – It is measured eastward along the celestial equator from the vernal equinox. It can be thought of as a projection of earths longitudes on the celestial sphere.
    2. Declination (δ) - measures an object's position north or south of the celestial equator. It is akin to latitude on Earth.
- Observer-Centered Definitions

    1. Horizon – The apparent boundary below which the sky will not be visible to the observer at a specific place on earth.
    2. Zenith – The point on the sky directly over our head.
    3. Altitude or Elevation – Angular height of an object above your horizon at any given moment.
    4. Azimuth – The azimuthal angle of an object in the sky relative to an observer. For objects exactly on North, East, West, and South, the azimuth angles will be 0, 90deg, 180deg, and 270deg respectively.
    5. Hour Angle (HA) – An object's HA is the amount of time (in hours) since the object transited.
    6. Local sidereal time (LST) – This is defined as the RA of the meridian. It is useful to keep track of the time of transit of various objects.

$$HA = LST - RA$$

1.3 Apparent Sizes and Solid Angle

Solid angle of an object in the sky is defined by

$$\Omega = \frac{A}{d^2}$$

Where A is the cross sectional area of the object d is the distance from observer to the object and for small angular sizes, it can be approximated by

$$\Omega = \frac{\pi}{4}\theta^2$$

These solid angles of various sources can be compared among various sources to find relevant properties.

1.4 Radio Telescope

Essential components of a radio telescope include
1. Parabolic Reflector: Also known as the dish, it collects and focuses the radio light to the receiver. Since these telescopes operate at longer wavelengths, they donot require highly polished or metallic surfaces, often a porous or mesh like structures would work as a good reflector. The size of the Reflector on the other hand plays a crucial role, in determining the amount of power received from a source. As we know sensitivity is proportional to the diameter squared.
2. Mount: it is the physical structure, with motors, that holds and moves the dish. All modern radio telescopes have altitude-azimuth or Alt-Az mounts which pinpoint receivers based on the altitude and azimuth of source. The other type of mount is the equatorial mount, which pinpoint based on the RA and Declination of the source.
3. Feeds, Recievers, and Computer: A feed is a specially designed antenna which converts EM waves into confined EM waves inside transmission lines. These signals then pass on to the receivers. Each feed is connected to a receiver feed staying on the dish and they are together called a Detector. Signals then are transmitted to the computer in electronic form for further data processing.

1.5 Radio Maps

Gray scale and false color radio map contours are two visual representations commonly used in radio astronomy to depict the intensity or distribution of radio signals received from celestial objects. In a gray scale radio map, variations in signal strength are represented by shades of gray, with darker shades indicating higher intensity regions. This allows for a visual assessment of the relative strength or concentration of radio emissions across the observed area. On the other hand, false color radio map contours employ a color scale, assigning specific colors to different intensity levels. This color coding provides additional information, making it easier to distinguish between various regions of interest or to highlight specific features in the radio emission. By utilizing these techniques, astronomers can effectively analyze and interpret the complex radio data, revealing intricate structures, hotspots, or faint emissions that might otherwise be challenging to discern in raw radio images.

1.6   FITS Handling and Imaging

As a part of gaining experience with obtaining and retrieving necessary information from the fits files, the following 3 galaxies are selected and their images in visible, IR and Radio wavelengths are plotted. Contrary to traditional beliefs, new phenomena and new entities can be observed from the different image of each galaxy.

1. **M87** Radio image of m87 highlights a jet of gases or other emmission from the core of the galaxy. While the IR and visible wavelength images have their brightest spots near the centers, the IR one is more diffused than the visible one indicating that there are some kind of objects in the galaxy which can act as a continnum of ir source, while thats not the case with visible image.
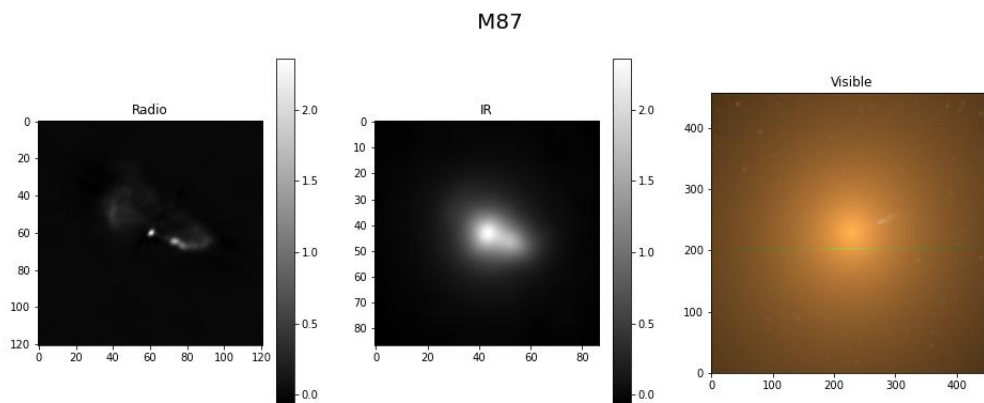
Figure 1.1: Radio, IR, and Visible Images of M87 Galaxy

2. **3C403** Radio image similar to above one reveals a cloud of gases like a remnant of supernova explosion (actually its a water megamaser) and this cloud of gases has no correlation to the stars we observe optically. The IR image reveals that few point sources among the bunch of stars seen from the visible image are capable of emitting strong IR radiation.

Figure 1.2: Radio, IR, and Visible Images of 3C403 Galaxy

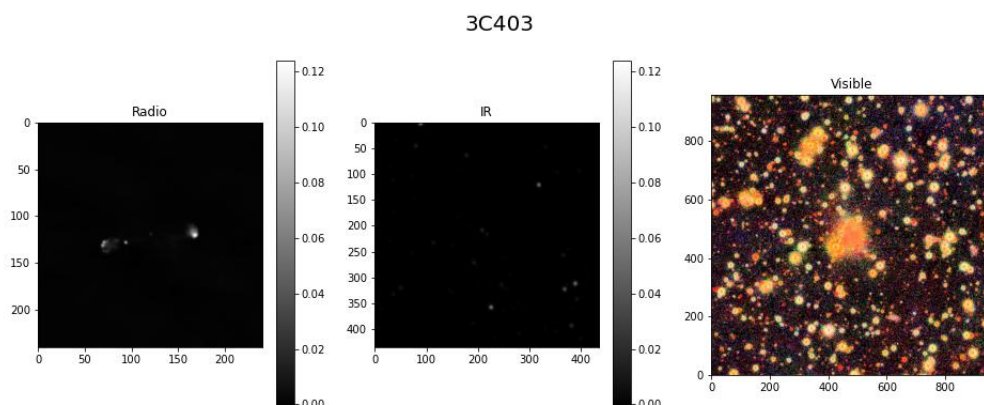3. **UGC595** An internet search revealed that this UGC00595 is a galactic nucleus, and we observe a faint radio jet being emitted along an axis of the center of nucleii, whose proportions might indicate its small age. Some stars are visible clearly in IR while some are clearly seen in visible images each complementing other. Nevertheless the central object is a strong emitter in all three wavelengths.
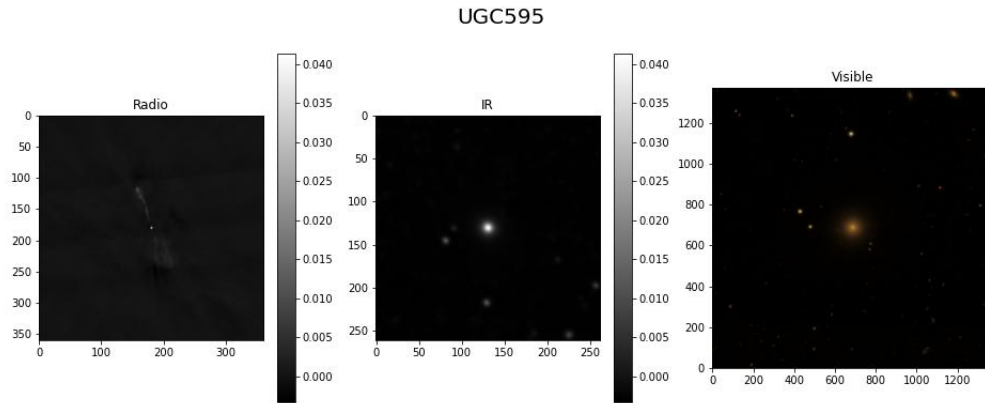

Figure 1.3: Radio, IR, and Visible Images of UGC595 Galaxy

1.7 Plotting Jet Afterglow Curve

A light curve or a Jet afterglow curve is the plot of flux density vs time. These plots play a crucial role in identifying any stellar events like supernova explosions etc. GW170817 was a merger of two neutron stars that was accompanied by both gravitational waves and electromagnetic radiation. To study this event, We used the data for the non-thermal emission from this source that spans across all frequency bands following a single spectral index of $F_\nu \propto \nu^{-0.584}$. The quantity F_ν is the flux density, And from the given dataset, compiled by Makhathini et al. (2021), The light curve was extracted and plotted.
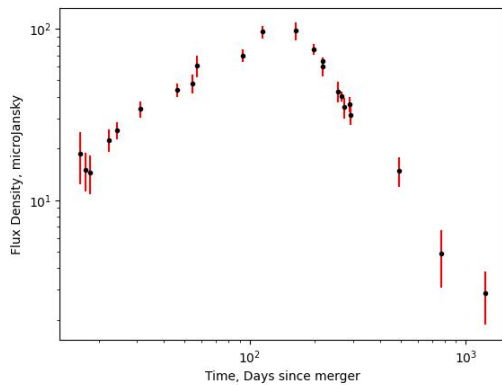

Figure 1.4: Light curve obtained from VLA Telescope
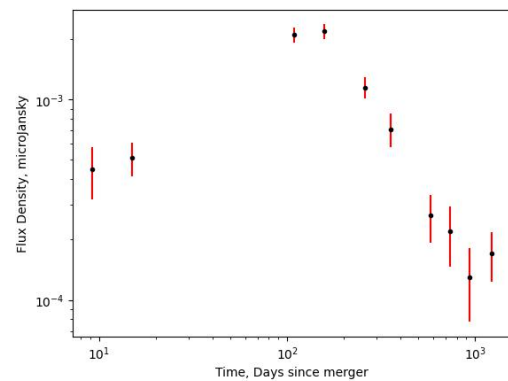
Figure 1.5: Light curve obtained from Chandra X-Ray Telescope

Similarly the data of same event observed from the Chandra X-Ray Telescope is also plotted after converting the flux densities from X-ray frequencies to Radio frequencies. This is done to essentially compare both plots at the end
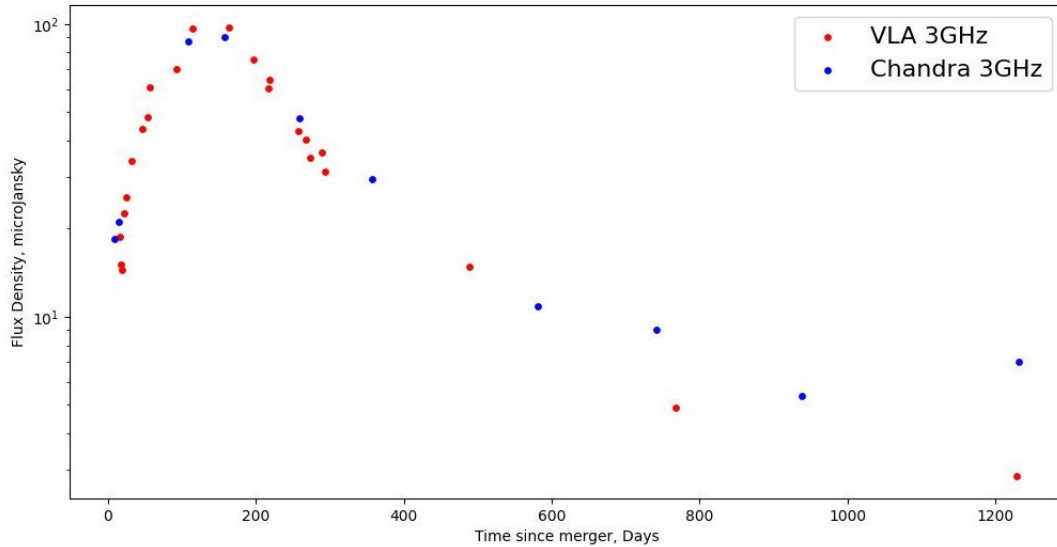
Figure 1.6: Light curve obtained from VLA Telescope

Despite operating in different wavelength ranges, the flux density data obtained from both telescopes show a consistent agreement, highlighting the robustness of the measurements. The VLA's radio observations and the Chandra's X-ray observations reveal complementary aspects of the event. The remarkable agreement between the VLA and Chandra observations showcases the power of multi-wavelength observations, allowing astronomers to gain a more comprehensive understanding of cosmic phenomena

2. Introduction to Radiation Physics

2.1 Important Quantities in an Observation

The Total Energy emitted indicates the same, total energy we get from a source over its whole lifetime or in a finite time period of measurement. For a universal measurement we can instead adopt Power as a better parameter. Power being the amount of energy obtained over a unit time period. The power obtained from EM radiation can also be termed as Luminosity. A catch with luminosity is that a single antenna designed to capture radio frequency cannot catch light of all visible, IR and other bands. So isolating power obtained from specific bands will be a more direct quantity obtained from telescope. The areas of the telescopes used for astronomy are not of the same type and we have known that area of telescopes affect the power received, hence a new quantity Flux is introduced as the amount of light energy per unit time per unit area. Considering a spherical shell of radius d, around the source, its power emitted will be,

$$P = \frac{L \, A_{eff}}{4\pi d^2}$$

and the Flux is given as

$$F = \frac{L}{4\pi d^2}$$

And Flux density is given as the Flux obtained over a fixed wavelength band or fixed frequency band, and both quantities are not same and are to be converted into one another using the given formula

$$F_\nu = \frac{F}{\Delta \nu}$$

$$F_\lambda = \frac{F}{\Delta \lambda}$$

And this flux density is what we obtain from the telescope. F_ν has a unit of 1 Jansky $1 Jy = 10^{-26} W m^{-2} Hz^{-1}$ Intensity (Surface brightness): It is defined as the Flux density

of the source per unit solid angle. And Intensity is of two types, I_ν and I_λ defined as follows. This intensity is what we compare between two sources when we say one is bright and the other is dim. Some important points about intensity,

- Flux density, F_ν, does not distinguish between the directions that the photons come from or travel to, whereas I_ν does. The directionality of the photons is important when studying the transfer of radiation through material, such as clouds of interstellar gas.
- Intensity is independent of distance. Intensity has two separate dependences on distance, in flux density and solid angle and they cancel with one another.

$$I_\nu = \frac{L}{4\pi\Delta\nu\,A}$$

- • Intensity is a direct measure of the object's surface brightness. Since intensity is independent of distance, the intensity one measures on Earth will be the same as that measured right at the surface of source.
- • This Intensity observed is related to the Electric (or Magnetic) Field Amplitude of the EM Wave as follows. This result follows from the derivation in electrodynamics.

$$I_\nu \propto E_0^2$$

2.2 Blackbody Radiation

The understanding of light as both waves and particles was a significant breakthrough in physics during the early twentieth century. Light exhibits wave properties such as interference and diffraction, while its energy is quantized into discrete units called photons. This realization originated from Max Planck's observation of quantized energy units in the radiation emitted by hot, opaque objects, leading to the concept of blackbody radiation.

When a hot object emits light, it transfers energy and cools down. The light we observe from objects often consists of both emitted and reflected light. The perceived color of objects is determined by the frequencies of light they reflect. To isolate the emitted light and study it separately, the notion of an opaque black body was introduced. A black body absorbs all incident light, reflects nothing, and prevents light transmission. The radiation emitted by a black body, known as blackbody radiation, is used as a model to investigate the fundamental properties of light and energy transfer in various systems.

Blackbody radiation refers to the maximum amount of radiation an ordinary body emits as it tries to cool. The total radiation emitted by a cooling body is not the sum of individual emission processes, as particles can also absorb radiation. The amount of radiation depends on the number of particles in the body, as more particles can emit more photons in each second. However, a larger number of particles increases the likelihood of some emitted photons being absorbed by other particles, causing an exchange of energy between photons and particles. The interaction between photons and particles is crucial for the resulting radiation.

The photon cloud, created by the matter particles, contains more energy than the radiating body, and the hottest photon cloud can reach when it has the same

temperature as the radiating body. The resultant radiation is a cloud of photons at thermal equilibrium with the body itself. When radiation is described as a cloud of photons at a specific temperature, it means that photons, as particles, follow Bose-Einstein statistics. Photons are bosons, distinct from fermions like electrons and protons. Statistical mechanics concepts such as Bose-Einstein statistics help describe the distribution of energies among thermalized photons. This distribution determines the relative number of photons carrying different energy ranges in blackbody radiation. The photons achieve a thermal equilibrium with the radiating particles due to their interactions within the opaque medium, leading to both having thermal energy distributions described by the same temperature.

The energy distribution function of the photons, $N_{ph}(E)$, directly relates to the spectral distribution function, which represents the intensity versus frequency. Since frequency is proportional to energy ($E = h\nu$ for photons), the intensity at a given frequency corresponds to the flux of photons at that frequency. By starting with the energy distribution function for a thermalized ensemble of photons, it is possible to convert it into intensity as a function of frequency. The passage mentions the Planck function, which describes this conversion, but does not provide the derivation. The key point is that the energy distribution function of photons is directly connected to the spectral characteristics of the radiation. The planck function given as follows will describe the spectrum emissions of blackbodies, and plots of these functions are given below,

$$B_\nu(T) = \frac{2h\nu^3}{c^2} \cdot \frac{1}{exp(h\nu/kT) - 1}$$

and similarly

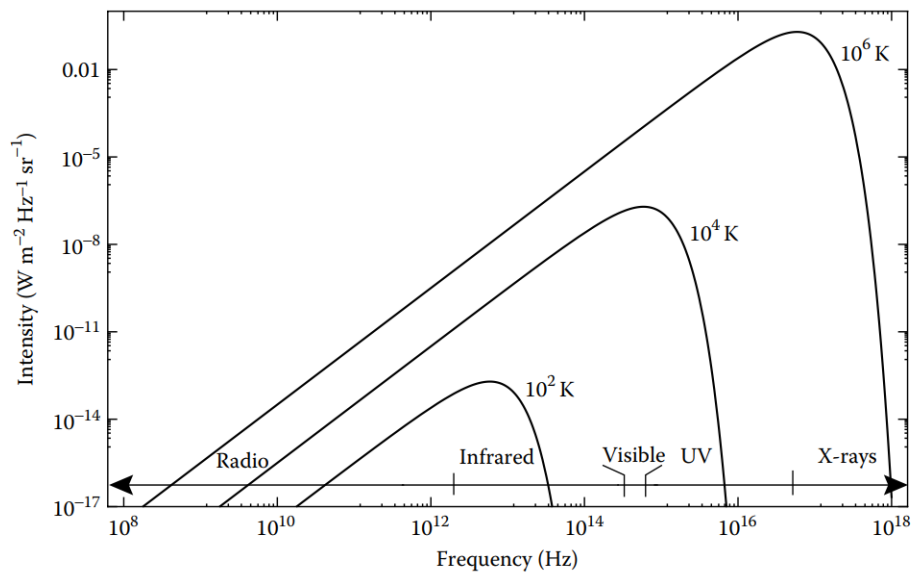$$B(T) = \frac{2hc^2}{\lambda^5} \cdot \frac{1}{exp(hc/\lambda kT) - 1}$$

Figure 2.1: Log-log plot of $B_\nu(T)$ versus ν for three different temperatures
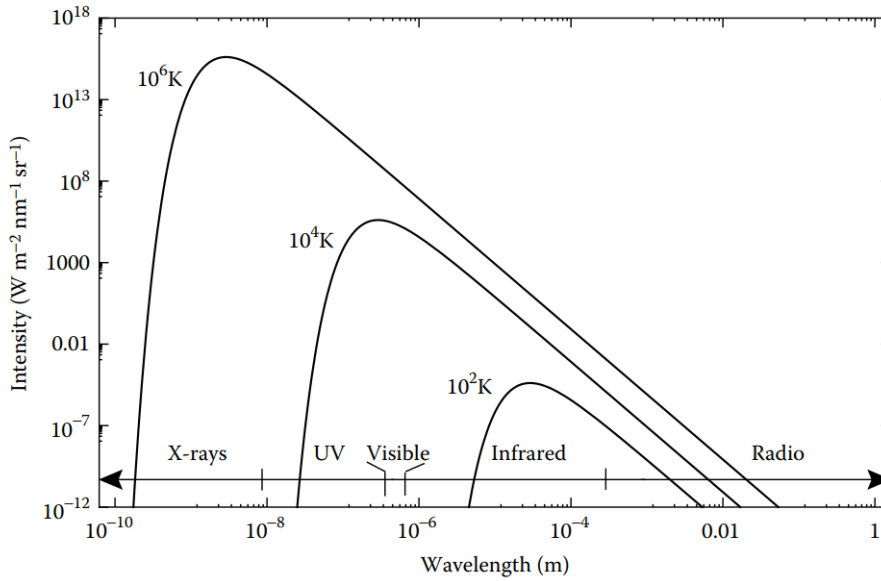
Figure 2.1: Planck function, plotted as B_λ, for the same three temperatures

And by integrating the planck function over its frequency and solid angle range gives us the Total Flux of radiation. Its relation with the temperature is given by Stefan-Boltzmann Law

$$F = \sigma \cdot T^4$$

An interesting consequence of knowing that the Cosmic Microwave Background (CMB) is a blackbody source, is that we could infer its temperature from a single frequency observation ie., observe the radiation from an empty patch of sky. And finally, if a body lacks sufficient particles to produce a distribution of photons equal in temperature to itself, it cannot create a photon cloud with a higher temperature than its own. Consequently, the photon cloud will have a lower energy density than the radiating body. As a result, some photons will escape the body before thermal equilibrium is achieved, rendering the body partially transparent and disqualifying it as a blackbody. This implies that an opaque body emits more intense radiation than a transparent body. The Planck function, denoted as $B_\nu(T)$, describes the maximum intensity that a radiating body of a given temperature will emit through thermal processes at each frequency. In essence, $B_\nu(T)$ represents the maximum intensity achievable by thermal radiation from an object at any wavelength, and any actual intensity $I_\nu(T)$ will be less than or equal to $B_\nu(T)$.

2.3   Relation between Intensites of Frequency and Wavelength bands:

Utilizing the fact that the total power radiated over the whole spectrum must be the same for both Intensity variables,

$$\int_0^\infty I_\lambda \, d\lambda = \int_0^\infty I_\nu \, d\nu$$

$$I_\lambda = \frac{c}{\lambda^2} \cdot I_\nu$$

2.4 Obtaining Temperature of CMB

The cosmic microwave background (CMB) has its properties closely modelled by a blackbody meaning, we can use the planck distribution functions and its corresponding results to find the temperature of the radiation source, here the CMB itself. To do so, infrared data adapted from the COBE satellite (Mather et al. 1990) is used to fit a blackbody curve to the CMB data. Initially the values of B_λ obtained from the raw data is plotted along with frequency to verify blackbody characteristics. If true it should match figures 2.1 and 2.2. The plots are displayed below.
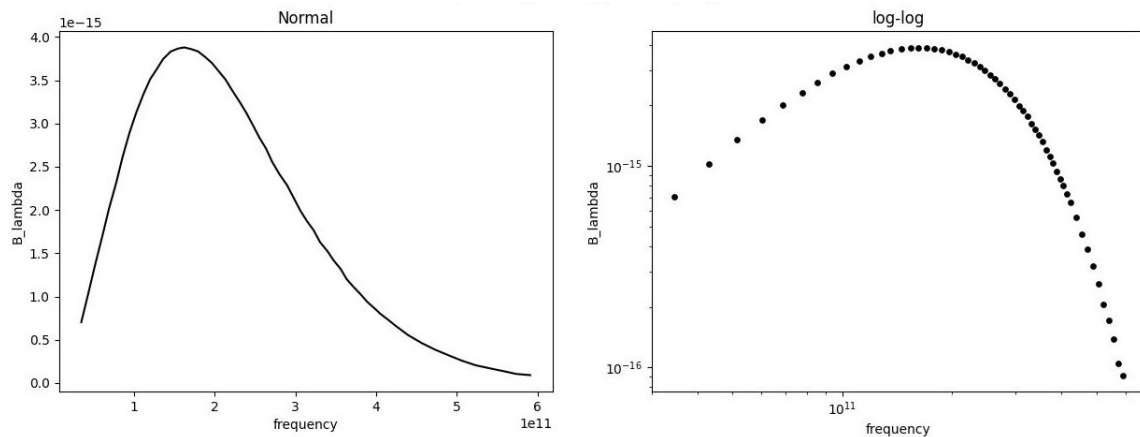

Figure 2.2: Plot of $B_\lambda(T)$ versus ν, COBE-CMB Data

Further the planck function is fit to the data points using scipy's curve-fit function, and it is worth noting that, when the parameters to be passed are too big or too small (which can happen quite often in astronomy), it is advisable to provide the curve-fit funtion with intital fit values with a closer order of magnitude for an accurate and successful fit.

After the fit parameters are obtained, it is elementary to obtain the CMB temperature. Here it was obtained as $2.739K$ which is close enough to the actual temperature.

2.5 Plotting Galaxy Rotation Curves

The galaxy rotation curve refers to the plot of the rotational velocity of stars or gas as a function of their distance from the galactic center. In a typical galaxy, such as our Milky Way, the rotation curve exhibits an unexpected behavior. According to the laws of Newtonian physics, one would expect the rotational velocity to decrease as the distance from the center increases due to the declining gravitational pull. However, observations have shown that the rotation curve remains nearly constant or even increases with distance, indicating the presence of unseen or "dark" matter. This suggests that there is a significant amount of invisible matter distributed throughout galaxies, exerting gravitational forces that counterbalance the expected decrease in rotational velocity. The galaxy rotation curve is crucial for understanding the nature and distribution of dark matter, and it challenges our current understanding of galactic dynamics.

To plot GR Curves, here we made use of the Hydrogen-21 cm spectral line data, which forms an essential part of any radio astronomy observation taking place today. The observed wavelengths of the 21cm H-lines are different from the wavelength of line emission calculated using quantum mechanics. This happens because of the relative velocity between source and observer and it is termed as the doppler shift (redshift commonly). And from the redshift data, relative (radial) velocity can be obtained thus providing us with the galaxy rotation curve.
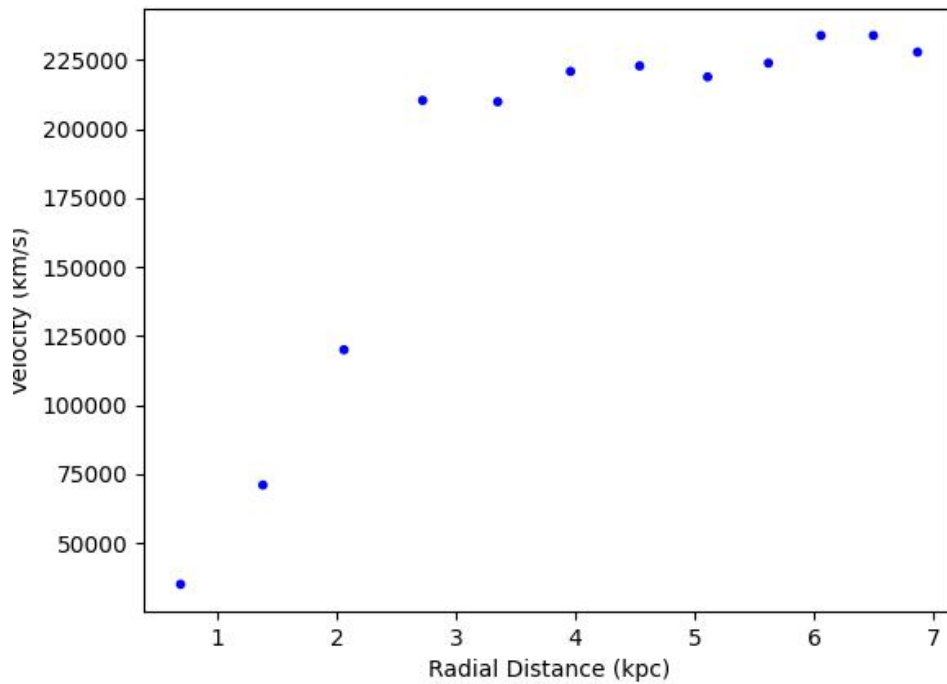The curve thus obtained is plotted below.

Figure 2.3: Galaxy Rotation Curve obtained out of simulated galaxy data

3. Radio Telescopes

3.1 Reflectors, Feeds and Recievers

A radio telescope is a fully steerable device mounted on Alt-Az mounts, which can point to any direction in the sky. It is controlled by a computer that continuously translates the sky coordinates of an astronomical object into current altitude and azimuth positions. Some aspects of a radio telescope are common to those used at ultraviolet, visible, or infrared wavelengths, such as the use of a primary reflector (and a secondary one too). However, there are significant differences in the method of light detection. At shorter wavelengths, the particle nature of light, meaning individual photons, is detected. This is how CCDs (widely used in cameras) actually work.

At very short radio wavelengths, new semiconductor and superconductor devices, such as kinetic inductance detectors, can detect individual photons. But understanding the detection of radiation at radio wavelengths requires understanding large ensembles of photons and utilizing the wave nature of light.

At radio wavelengths, coherent signal processing is used, using heterodyne receivers and incoherent power detectors (bolometers) are also used at submillimeter and millimeter wavelengths. Broadband photometry detects thermal radiation from stars over broad wavelengths, while spectrometers measure power across narrow frequency bands. Radio telescope spectrometers are used to measure power across narrow adjacent bands, different from visible and infrared wavelengths.

3.1.1 Reflectors

Radio telescopes use parabolic reflectors, similar to primary components in infrared, visible, and ultraviolet regimes. These reflectors cause waves approaching the dish from perpendicular to the entrance plane to come to a single point, known as the focus. The EM waves emitted by an astronomical object are well-

approximated as plane waves and enter the telescope in parallel paths. Two methods for representing light paths are ray tracing and wave-front tracing. In a visible-wavelength telescope, a CCD camera is placed at the focal plane to obtain an image of the object.

At the focal plane, feed horns convert EM waves from free space to transmission lines, allowing the signal to travel to receivers. Most radio telescopes are of Cassegrain design, with a second reflector placed before the primary reflector to redirect waves to another focal point. Most large radio telescopes are classical Cassegrain telescopes, which use a parabolic primary and hyperbolic secondary.

The primary reflector plays two crucial roles in a radio telescope. It collects and focuses radiation from astronomical sources, making faint sources more detectable. The effective area (Aeff) depends on the telescope's physical area, with larger reflectors collecting more power and detecting fainter sources. Directivity, the ability of a telescope to differentiate emission from different angular positions, determines the resolution in a map. Directivity is largely dependent on the primary reflector's diameter and is governed by diffraction, which limits the directivity of all telescopes.

3.1.2 Beam Pattern

The beam pattern indicates the telescope's sensitivity to incoming radio signals based on the angle on the sky. It is similar to the point-spread function, which describes the sensitivity of a beam of radio waves leaving a transmitting antenna. However, diffraction, a phenomenon of all types of waves, occurs when waves pass through an aperture. The Huygens-Fresnel principle visualizes diffraction by imagining that each point along the wave front is the source of a secondary spherical wave, and the total wave front is the sum of these secondary wave fronts, taking into account wave amplitude and phase. The behavior of light as it reflects off the primary reflector of a telescope is closely related to the behavior of light passing through a single slit. The reflector acts like a circular aperture, and the interaction of light waves meeting at the focus is identical to that when light passes through a circular aperture and meets at a spot on a wall.

For sources lying directly on the axis, we see the incoming waves adding constructively at the focus owing to the symmetry of paths, but in case of sources aligned slightly off the axis, we find a path difference of $\Delta s = L \cdot sin(\theta)$, for L being the separation between the ends of a telescope (diameter). And for a very little off-axis tilt, we can approximate $sin(\theta)$ θ, thus resulting in $\Delta s = L \cdot \theta$. Thus the corresponding phase difference accounting to the path difference is

$$\Delta \phi = 2\pi \cdot \frac{L \cdot \theta}{\lambda}$$

Substituting path difference of $\lambda/2$ for destructive interference, we find $\theta = \lambda/2L$. These equations along with standard derivations in optics, we get the sensitivity patterns called as Airy patterns, used to define a telescopes angular resolution. Such a pattern is given in the figure below. This pattern consists of a central big lobe (main lobe), and other small lobes (side beams) separated by minimas caused by destructive interference. The first minima is calculated to occur at $1.22\lambda/D$ marking

the limit of resolution of telescope this definition of resolution applies widely for visible-wavelength telescopes. For radio telescopes, we consider the FWHM of the main lobe as the limits of resolution. For example, the angular resolution (denoted as FWHM angle) with the optimum (10-dB) edge taper, the angular resolution is

$$\theta_{FWHM} = 1.15\frac{\lambda}{D}$$

3.1.3 Surface Errors

A radio telescope's primary reflector is imperfect, with manufacturing imperfections limiting surface accuracy. These imperfections cause slightly different path lengths to the focus, reducing power collected. The total path difference is twice the deviation, resulting in rms phase errors of $4\pi dz/\lambda$. Effect of surface errors on the collecting area is given by the Ruze equation

$$A_\delta = A_0 e^{(4\pi\delta z/\lambda)^2}$$

The Ruze equation calculates the fractional loss in collecting area in terms of surface deviations in units of the observing wavelength. A reflector should have rms surface errors less than 1/20th of the wavelength of the light being detected for reasonable performance. Radio telescopes need to be larger to achieve useful resolution, making meeting this constraint difficult. Surface irregularities cause a loss of sensitivity by transmitting radiation off these deviations into a large beam with angular size of order /dx. This sensitivity pattern, called the error pattern, involves not only unwanted sidelobes but also error patterns.

The error pattern has a larger angular scale than the main beam, causing a significant amount of total power loss. Additionally, larger scale deformations of the reflector due to gravity introduce errors with larger length scales than manufacturing errors, producing error patterns on smaller angular scales. In summary, the effective collecting area of a telescope is smaller than the physical area of the reflector due to limited surface accuracy, illumination pattern, and physical blockage.

3.2 Noise, Noise Temperature and Antenna Temperature

Nyquist in 1928, for example, found that a resistor in the circuit will add electrical noise with a power per Hz that depends solely on the resistor's temperature. For this reason, the electronic power in a circuit, in general, can be described in terms of an equivalent temperature, T_{equiv}, which is equal to the temperature of a resistor that would produce the same amount of power as the resistor. Following this convention, radio astronomers also describe the power traveling in the transmission lines and receiver in terms of an equivalent temperature given by

$$T_{equiv} = \frac{P}{k\Delta\nu}$$

The antenna temperature (TA) is the equivalent temperature of the power delivered to the transmission line by the antenna. The majority of detected power is due to noise from receiver components, with total noise power (TN) describing the total noise power. The final power measured in the receiver output relates to the

antenna temperature and noise temperature of each component. The equivalent temperature of the final power output is not simply the sum of the equivalent temperatures of all sources in the path. The source signal is affected by the receiver processes, with gain (G) for each step. And we get the total noise temperature by equating total power to the sum of the powers for each component. The result is obtained in the following expression. This total noise temperature is also called as the receiver noise temperature.
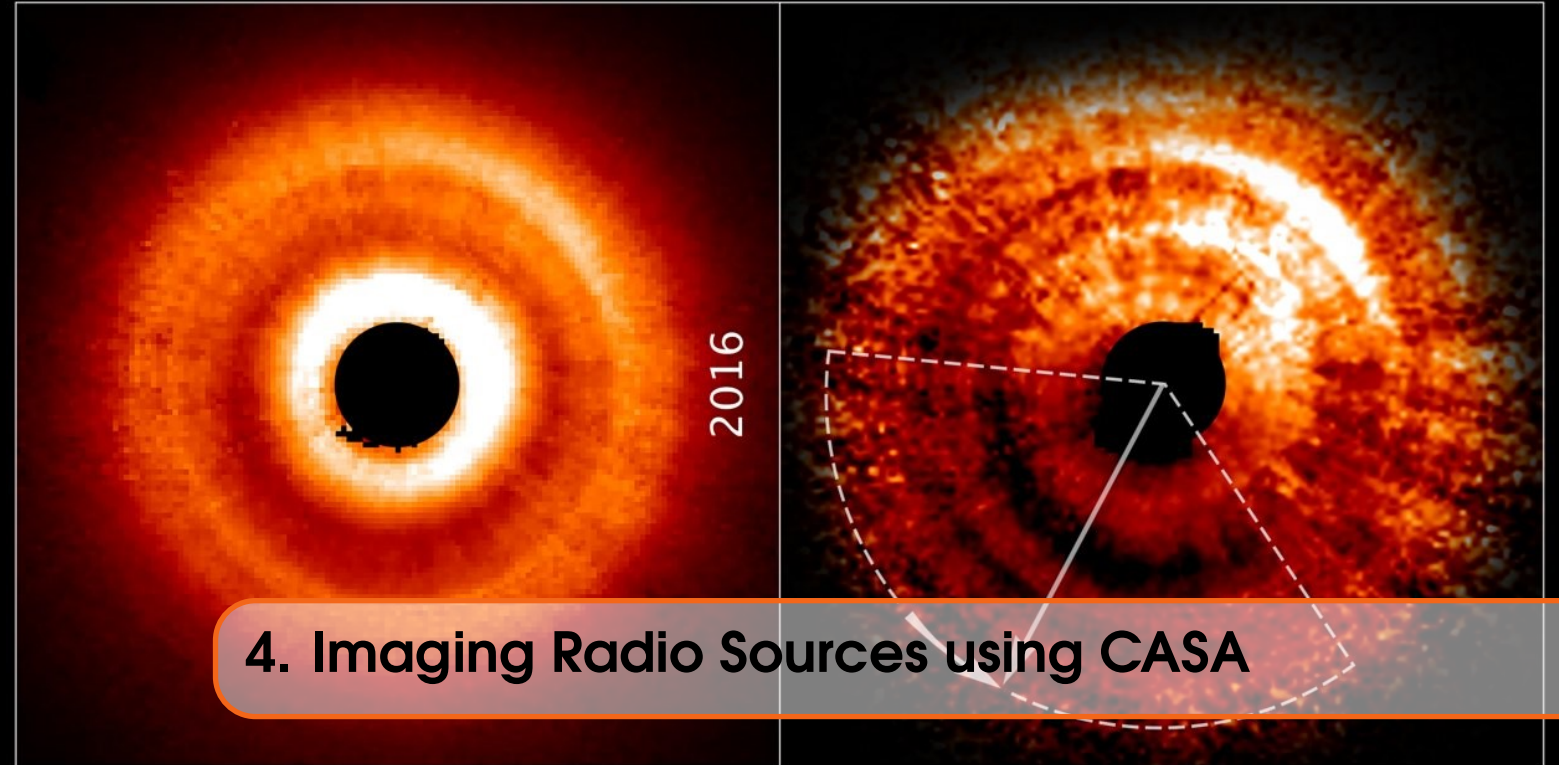
$$T_N = T_{N1} + \frac{T_{N2}}{G1} + \frac{T_{N2}}{G1G2} + \dots$$

A lossy element, like a mixer or transmission line, has a loss factor (G) less than 1, increasing the contribution to the total noise temperature from all components that come after it. This is because loss decreases the power in the source signal, making any noise generated later appear larger relative to the source signal. The noise contribution of each successive device to the total noise is reduced by the product of the gains of the preceding elements. The RF amplifier, the first device radiation enters immediately after the feed, is the most critical in determining the total noise temperature. With gains of at least a factor of 100, the contributions to the noise temperature of all other elements in the receiver and detector are reduced by at least a factor of 100. Most receivers on professional telescopes are cooled with cryogenic refrigerators to further reduce noise. Low-noise RF amplifiers are difficult to build at high radio frequencies, so making the mixer the first element can result in a smaller total noise temperature. However, high-frequency receivers have higher noise temperatures than those at lower frequencies.

Astronomical sources and receivers have a tolerance of TA « T N, making total power measurements difficult. Instead, switched power measurements are used to measure the difference in voltage between on-source and off-source observations. These observations remove the offset caused by noise power, but fluctuations in noise power still affect measurement and dominate the uncertainty in antenna temperature. These fluctuations limit the sensitivity of a radio telescope to detect faint astronomical sources. The variance of noise signals, focusing on the variance of noise power, is a significant factor in determining the sensitivity of a radio telescope to detect faint astronomical sources.

The variance depends on two effects: fluctuations in the photon arrival rate and wave noise. The uncertainty in the measure decreases by averaging more values and increasing the bandwidth. In an observation with a bandwidth of D_v and integration time of D_t, the uncertainty in the power measured, σ_P, is given by

$$\sigma_P = \frac{P_N}{\sqrt{\Delta t \cdot \Delta v}}$$

2016

4. Imaging Radio Sources using CASA

4.1 Additional Concepts in Radio Observations

Radio observations of astronomical phenomena are generally taken from two types of telescopes, Single Dishes constitute one type while the Aperture synthesized arrays of smaller telescopes together form the second type. Single dish radio telescopes consist of a large, single parabolic dish that collects radio waves and focuses them onto a receiver. These telescopes are efficient for capturing large-scale emissions and conducting surveys of the sky. However, they have limited resolution due to the diffraction limit, which affects their ability to resolve fine details in the observed objects.

On the other hand, aperture synthesis methods involve combining the signals from multiple smaller antennas spread over a wide area to achieve a virtual larger aperture. This process creates an interferometer, allowing for high-resolution imaging. The individual antennas act as elements of a larger, synthesized telescope, providing enhanced spatial resolution and the ability to observe fine structures in distant sources. Aperture synthesis techniques enable astronomers to produce detailed radio maps with exceptional clarity and sensitivity. In summary, single dish radio telescopes are efficient for broad surveys and observing large-scale emissions, while aperture synthesis methods offer superior resolution.

4.1.1 Single Dish Radio Telescopes

Unlike optical telescopes, which utilize mirrors to collect visible light, radio telescopes employ large parabolic dishes to gather and focus radio frequency (RF) radiation from space. And the total power collected by the dish is given by the expression below, neglecting all other complications in the process (like switched power observations).

$$P = F_\nu \cdot A_{eff} \cdot \Delta\nu$$

This leads us to On-Source, Off-Source Voltages and gain,

1. **On-Source Voltages:** The "on-source" voltage refers to the electrical signal recorded by the receiver system when the telescope is pointed directly at the celestial source being studied. It represents the total signal received from the target source, including any radio emissions or reflections coming from it.

$$V_{on} = \alpha G k \Delta v (T_{sys} + T_A)$$

2. **Off-Source Voltage:** Conversely, the "off-source" voltage is the electrical signal recorded by the receiver when the telescope is directed away from the target source, typically towards a region of the sky that is believed to have no significant radio emission from the source of interest. The off-source voltage serves as a reference or baseline measurement to account for background noise, instrumental effects, and other extraneous signals not related to the target source.

$$V_{off} = \alpha G k \Delta v T_{sys}$$

Here T_{sys}, and T_A are called the system and antenna temperatures. By taking the difference between the on-source voltage and the off-source voltage, we can effectively remove unwanted noise from the data, leaving behind the true signal emanating from the celestial source. This process is known as "background subtraction" or "baseline correction,"

Apart from this we also need to take care of the telescopes 'Gain' to properly proceed observing, It is a crucial parameter in radio telescopes that represents the sensitivity and efficiency of the telescope in collecting radio signals. It is a measure of how effectively the telescope converts incoming radio waves into electrical signals that can be recorded and analyzed. A high gain implies that the telescope is highly efficient at collecting signals, while a low gain indicates reduced sensitivity. Gain calibration is essential for accurately interpreting the received signals and quantifying the intensity or flux of radio emission. And this calibration is done from comparing the voltages from a known source beforehand. How ever, in this case, the gain is time dependent and we follow a method called 'Dicke Switching' to obtain signals.Dicke switching is a technique employed to distinguish between the on-source and off-source signals, which is crucial for background subtraction and baseline correction. The Dicke switch is an electronic device that rapidly alternates the telescope's focus between the on-source position (target source) and the off-source position (a reference position with no significant radio emission from the source of interest). During Dicke switching, the telescope switches back and forth between the on-source and off-source positions several times per second. The recorded voltages during these switching cycles are used to compute the difference between the on-source and off-source voltages.

Now with all this in hand, we plan the observation with help from parameters T_A and T_{sys}. Crudely we might get an approximation of Signal to Noise ratio (SNR) as T_A/T_{sys}, but a better way of getting reliable estimates is to use the radiometer's equation, which can be roughly written as,

$$\sigma(T_A) \propto \frac{T_{sys}}{\sqrt{\Delta t_{obs} \Delta v}}$$

And correspondingly the resolution of single dish telescopes is also dependent on

the wavelengths and its 'Diameter equivalent' as follows,

$$\theta_{res} = 1.15\frac{\lambda}{D}$$

Widely known SDRT's around the world include Green Bank, and the Arecibo radio telescopes having their diameters of 100m and 305m respectively. Although lacking behind in resolution, they are still an optimal resource to carry out broad surveys and sky mappings from time to time.

4.1.2 Aperture Synthesis

One major difficulty with single-dish telescopes is their resolution. With typical optical telescopes having resolutions upto 1 arcsecond, obtaining such a resolution for a radio telescope will require dish diameters being around 5kms. This requirement sets both engineering and operating difficulties to the device. One ingenious solution to this is to use arrays of smaller telescopes spread open in a wide area and combine their simultaneous observations using interferometry. This process is called Aperture synthesis. With this, we can achieve resolutions around the size of telescopes along the longest baseline. Considering a two telescope interferometry to observe a point sources for the ease of understanding, The electric fields at the two antennas are given as,

$$E_1 = E_0 \cos 2\pi \nu(t)$$

$$E_2 = E_0 \cos 2\pi \nu(t + \tau)$$

And the time delay between the two is caused by the path difference between the two, and is given to be,

$$\tau = \frac{\Delta s}{c} = \frac{b \sin \theta}{\lambda \nu}$$

Now the time averaged product of E_1 and E_2 gives the net signals from the source, which we can obtain as

$$< E_1 \cdot E_2 >= \frac{E_0^2}{2} \cos \left(2\pi \frac{b \sin \theta}{\lambda} \right) = \frac{E_0^2}{2} \cos \left(2\pi \frac{b \sin (\omega_E t)}{\lambda} \right)$$

This gives us a response signal which oscillates over time, a "fringe function". And the amplitudes of these fringes give us the Flux density of the point source. Apart from that Phase (position) calibration is done repeatedly (between scans of the target) by observing another bright source close to the source of interest. The fringe amplitudes combined with determined phase is given in the equation below.

$$R = F_\nu \cos \left(2\pi \frac{b \sin (\omega_E t)}{\lambda} + 2\pi \frac{b \Delta \theta}{\lambda} \right)$$

With all these known, deriving the visibility equation (given below) should be a trivial exercise. But the resulting equation holds more value to the observations than the derivation

$$V_{b/\lambda} = F_\nu \cos \left(2\pi \frac{b \sin (\omega_E t)}{\lambda} \right) = V_A \cos \Phi_V$$

Similarly for an extended source we get the observed visibility function (V(u, v)) in aperture synthesis from the Fourier Transform of the brightness distribution (I(x, y))

$$V(u,v) = \iint I_v(x,y) e^{(-2\pi i(ux+vy))} \, dl \, dm$$

4.1.3 Imaging with CASA

Once the data from observations is ready, the overall imaging process is just cleaning up the unwanted interference until a clear image of target is obtained. This will be done on a computer and CASA provides the tools required for this. The general methodology is provided here but to image accurately, it is necessary to regulate and extrapolate things until necessary quality is achieved.

1. Data Preparation: Ensure that your raw data files are in the correct format and have the necessary calibration information. Use CASA's data import functions to convert the data into CASA Measurement Set (MS) format. This step includes flagging and calibration of the data to account for instrumental effects and calibration sources.

2. Start CASA and Load Data: Open CASA by running the "casa" command in the terminal. Load your calibrated Measurement Set using the os.system() or importasdm() function. You can also use the listobs() function to inspect the contents of the Measurement Set and check the metadata.

3. Data Inspection and Flagging: Examine the data with tools like plotms() or plotxy() to inspect the visibility data and identify any issues or artifacts. Flag any problematic data points or unwanted interference using the flagdata() function.

4. Imaging: Use the clean() function to perform imaging and deconvolution of the data. Specify the necessary parameters such as the field of view, pixel size, and image size. The CLEAN algorithm will deconvolve the dirty image, resulting in a clean image of the radio source.

5. Primary Beam Correction (for VLA data): If you are working with VLA data, apply primary beam correction to account for the changing sensitivity across the field of view due to the VLA's array configuration.

6. Visualization and Analysis: Use CASA's visualization tools, such as viewer() or imview(), to view and analyze the resulting clean images. Apply any necessary image processing techniques like smoothing or masking to enhance the visibility of features in the image.

7. Export and Publication: Once you are satisfied with the results, export the clean images to common formats (e.g., FITS) for further analysis or publication.

Cleaning is the most crucial step in the whole imaging process, and it is done by first creating a "dirty" image by gridding the visibilities (measured data points in the Fourier domain) onto a regular grid in the image plane. The Fourier Transform of this gridded data yields a 2D image, known as the dirty image. The dirty image contains artifacts and sidelobes due to the irregular sampling of the visibilities and incomplete coverage of the Fourier plane. Then creating a "Point Spread Function", The PSF represents the response of the interferometer to an unresolved point source in the sky. It is obtained by imaging a calibrator source that is known to be a point source.

The CLEAN algorithm iteratively removes the point sources (components) from the dirty image, effectively deconvolving it. Starting from the brightest pixel in the dirty image, CLEAN subtracts the scaled PSF at that position and places a

model component (delta function) at that location. This process continues iteratively, searching for the next brightest pixel, until a specified threshold or number of iterations is reached. Each model component represents an approximate reconstruction of the original source's emission. After the deconvolution process, a residual image is obtained by subtracting the model components from the dirty image. The residual image contains the emission that is yet to be accurately represented by the CLEAN components.

And then the final clean image is generated by combining the CLEAN components and the residual image. The clean image represents the best reconstruction of the true sky brightness distribution.

4.2 Imaging TW Hydra protoplanetary disk

The dataset to image TW Hydra is obtained from the Atacama Large Millimeter Array (ALMA), and the data is precalibrated and pre-flagged by the providers to focus on the imaging part. And the imaging procedure is described below.

1. Firstly the complete data set (around 4.1GBs) is downloaded from the NRAO websites and the calibrated and flagged data is copied separately to working location.
2. Then the `listobs()` task is used to get an overview of the Fields, Calibrators and other smaller details of the observation.
3. Then the `listobs()` task is used to get an overview of the Fields, Calibrators and other smaller details of the observation.
4. Data is further inspected using the `plotms()` task to look at the u-v data in graphical manner, as well to observe the amplitude vs u-v distance plots. This is done to gain further insights over the data to be imaged.
5. Then you start the cleaning process by setting its required arguments, such as the image name, image size, deconvolver type, etc.,
6. Among the tclean's arguments, we set the image size to be 128x128px so as to fit it correctly, setting it too less or too more will render the image too pixelated thus defeating the entire purpose. As shown in Fig 4.1.
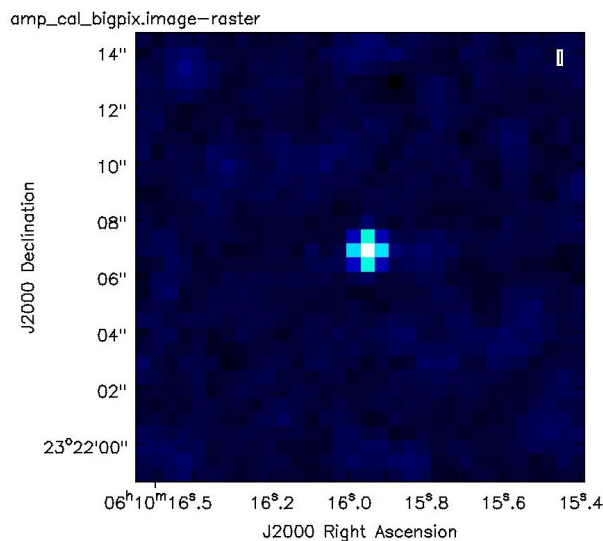

Figure 4.1: Image when less than adequate pixels are allocated while deconvolving

7. Then in the interactive window, Mask the target object of the image, ie., the protoplanetary disk using an elliptical mask option. Then deconvolve it until the emissions from noise around the disk and the masked area look somewhat similar. Thus the deconvolving process will be over.

8. Now the continuum emission data is separated from the whole by using the 'split()' method (with prior knowledge from 'listobs() task'), and is deconvolved again and imaged.

9. Then primary beam correction is applied to the imaged data using 'impbcor()' task in CASA. This is done just before exporting the image, and after all deconvolutions and analyses on the image are done. This is due to the convenience of working with images, but it is important to not forget applying this correction because the values of Fluxes and Flux densities depend on this.

The final image of the planetary disk is shown in Fig 4.2
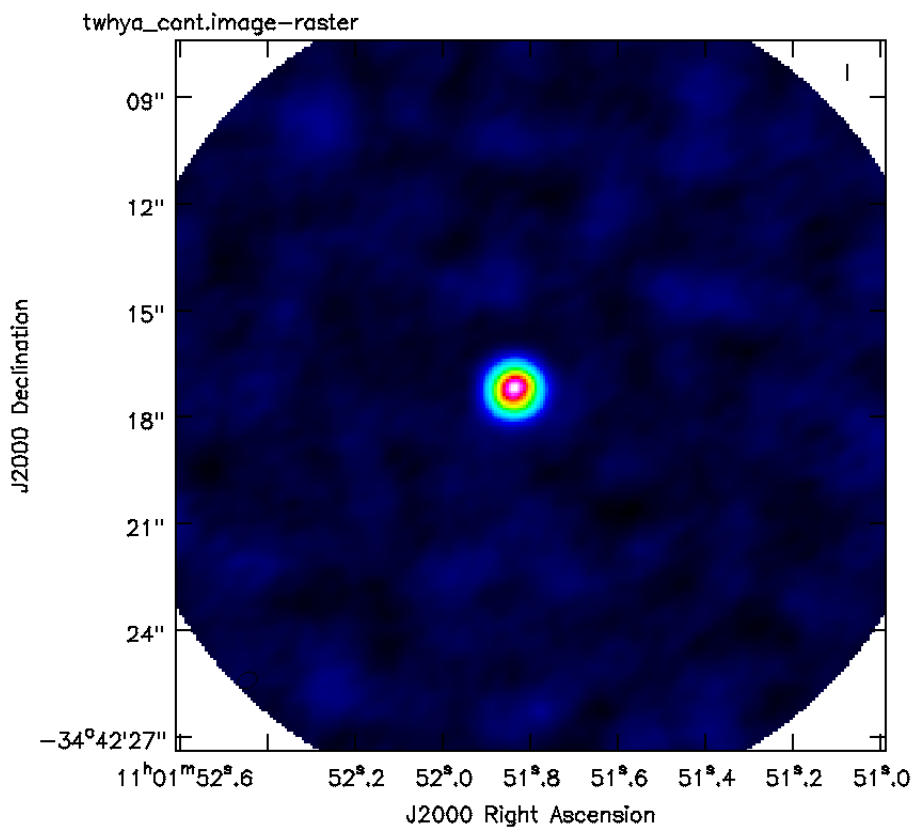
Figure 4.2: Final image after cleaning and primary beam correction

4.3   Imaging 3c391 Supernova Remnant

Similar to the above procedure, the image dataset for 3c391 is first calibrated and flagged, before proceeding with deconvolution. The graphical distribution of u-v data and Amplitudes vs u-v distance plots from 'plotms()', are displayed below.
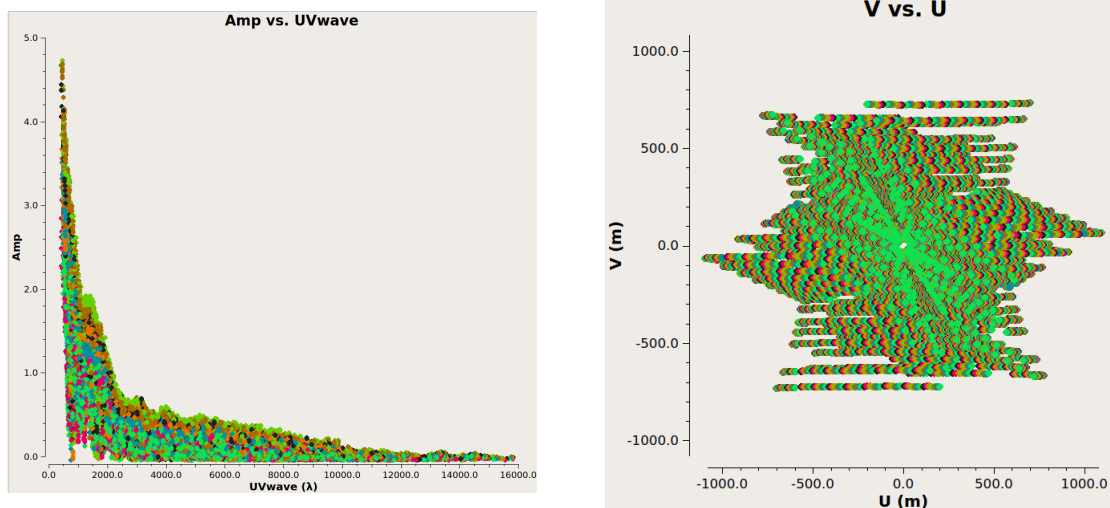
Figure 4.3: Results of Data Inspection using the task plotms

After deconvolving, splitting and primary beam corrections, the image of continuum emissions from supernova remnant is obtained as shown below.
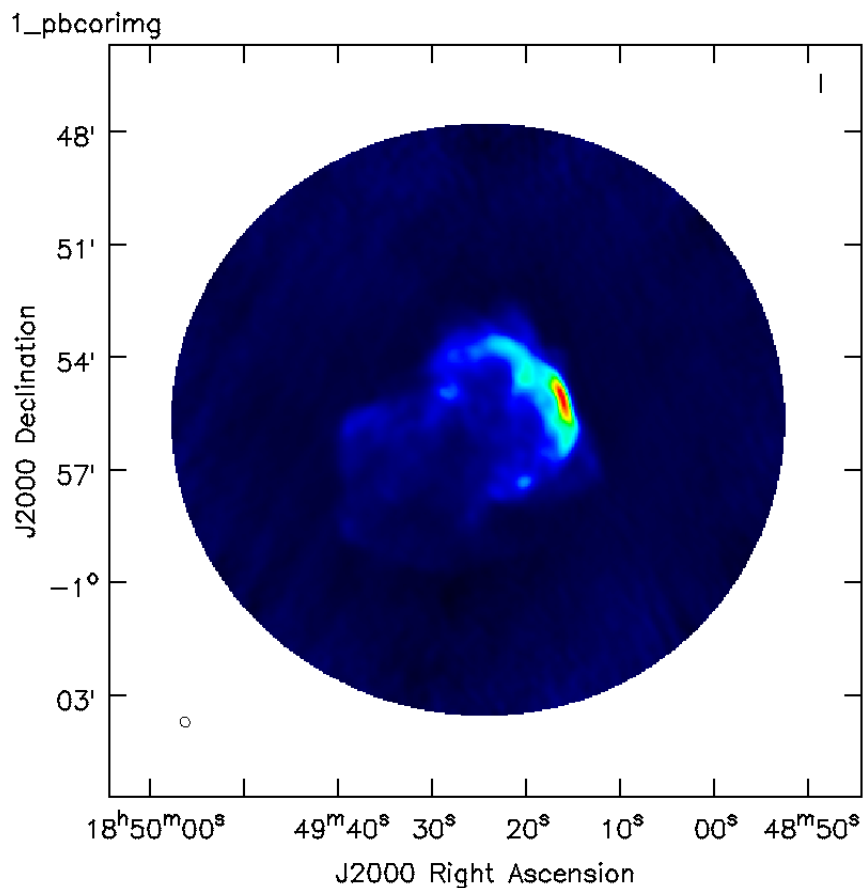

Figure 4.4: Final image after cleaning and primary beam correction

Alternatively, the task `imfit()` can also be used to fit a gaussian, by providing it with necessary image-ranges. Then the function tries to fit a 2D gaussian on the

image and that to calculate Flux and RMS values. And expectable, this method of getting flux only works for point sources, and it shows visible deviation from the correct values if used on any extended source. But the deviation is observed to be lower on circularly symmetric targets like TW Hydra disk.

The results of analysing supernova's flux densities are tabulated below.

Table 4.1: Results of image analysis

Peak Flux Density (F_p)	0.1531 mJy/beam
Flux Density	8.261 Jy
RMS	0.703 mJy
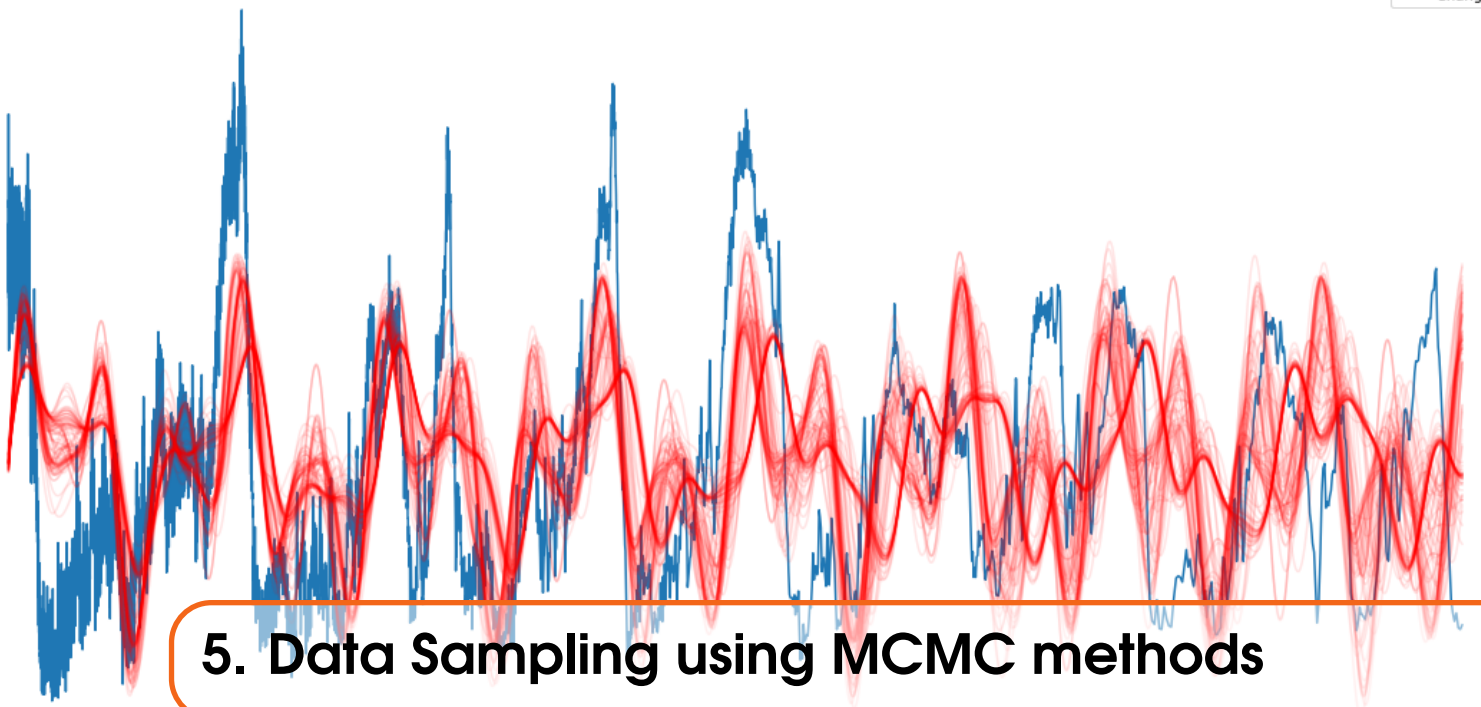
5. Data Sampling using MCMC methods

Markov Chain Monte Carlo (MCMC) sampling is a powerful statistical method used in astronomy data analysis to explore complex and high-dimensional parameter spaces. It is particularly valuable when dealing with models that cannot be efficiently solved using traditional mathematical methods. MCMC sampling allows astronomers to infer the most likely set of parameters that best explain the observed data and obtain uncertainty estimates for those parameters.

5.1 Introduction to MCMC Sampling

MCMC is a Bayesian statistical approach, meaning it relies on Bayes' theorem to update the probability distributions of model parameters based on observed data. The goal is to find the posterior probability distribution of the model parameters given the data, which is proportional to the likelihood of the data given the parameters and the prior probability distribution of the parameters. In astronomy data analysis, the model parameter space can be quite large and complex, containing multiple parameters that describe the physical properties of the observed objects or processes. MCMC sampling explores this parameter space to find the best-fit model parameters that explain the data.

The most commonly used MCMC algorithm in astronomy is the Metropolis-Hastings algorithm. It starts with an initial set of parameter values and proposes new parameter values based on a proposal distribution. The proposal distribution determines how far the algorithm will explore from the current parameter values.The proposed parameter values are accepted or rejected based on an acceptance-rejection criterion. The criterion involves comparing the likelihood of the proposed parameters with the likelihood of the current parameters, as well as incorporating prior information through the prior probability distributions.The accepted parameter values form a Markov Chain, where each set of parameters depends only on the

previous set. The Markov Chain explores the parameter space, sampling regions that have higher likelihood values, thus concentrating around the most probable parameter values.

Convergence is a crucial aspect of MCMC sampling. It is essential to ensure that the Markov Chain has explored the parameter space thoroughly and has reached a stable distribution. Several convergence diagnostics, such as the Gelman-Rubin statistic or trace plots, are used to assess convergence.Once the MCMC sampling is complete and the Markov Chain has converged, the posterior distribution of the model parameters is obtained. This distribution represents the best estimate of the parameter values that explain the data, along with uncertainties or confidence intervals.MCMC sampling allows for model comparison using the Bayesian evidence (marginal likelihood). By comparing the evidence for different models, astronomers can select the most appropriate model that best fits the data.

5.1.1   Implementing MCMC

Implementing Markov Chain Monte Carlo (MCMC) sampling involves several steps to fit a model to observed data and obtain estimates of the model parameters along with their uncertainties. Here are the key steps for implementing MCMC sampling of data:

1. **Choose a Model:** Select an appropriate model that represents the data you want to analyze. The model should have parameters that you want to estimate based on the observed data. For example, in astronomy, the model might be a smooth broken power law for a light curve.
2. **Define Priors:** Specify prior probability distributions for the model parameters. Priors represent your knowledge or beliefs about the parameter values before seeing the data. Priors can be uniform, Gaussian, or other distributions, depending on your understanding of the parameters.
3. **Compute Likelihood:** Calculate the likelihood of the observed data given the model and its parameters. The likelihood represents how well the model explains the data. For example, in the case of a light curve, you would compute the likelihood by comparing the model light curve with the observed data points, considering the uncertainties in the data.
4. **Define the Posterior Distribution:** Use Bayes' theorem to combine the prior probability distributions and the likelihood to obtain the posterior probability distribution of the model parameters given the observed data.
5. **Initialize the Markov Chain:** Start the MCMC algorithm by choosing initial values for the model parameters. These initial values can be randomly chosen or based on some prior knowledge.
6. **Proposal Distribution:** Specify a proposal distribution that determines how the MCMC algorithm explores the parameter space. The proposal distribution suggests new parameter values based on the current values.
7. **Metropolis-Hastings Algorithm:** Implement the Metropolis-Hastings algorithm or another MCMC sampling algorithm to generate a sequence of parameter samples. The algorithm iteratively proposes new parameter values, calculates their acceptance probability based on the likelihood and priors, and accepts or rejects the new values.
8. **Burn-in Period:** Run the MCMC algorithm for a burn-in period to allow the

chains to converge to the posterior distribution. During this phase, the samples might not accurately represent the true posterior.

9. **Sampling Phase:** After the burn-in period, continue sampling the parameter space to obtain a sufficient number of samples from the posterior distribution. These samples represent the best-fit parameter estimates and their uncertainties.

10. **Convergence Diagnostics:** Use convergence diagnostics, such as the Gelman-Rubin statistic or trace plots, to assess whether the chains have converged to the true posterior distribution.

11. **Post-processing:** Analyze the MCMC samples to obtain the parameter estimates and uncertainties. Compute summary statistics, such as the mean, median, and credible intervals, to characterize the best-fit model.

12. **Visualization and Interpretation:** Visualize the MCMC samples and the best-fit model to understand how well it fits the data. Interpret the results in the context of your scientific goals and draw conclusions based on the parameter estimates and their uncertainties.

Implementing MCMC sampling can be computationally intensive, especially for complex models and large datasets, but it provides a powerful and flexible approach for analyzing data and estimating model parameters in a Bayesian framework. Parts of this process can be implemented using a python framework called 'emcee'. This package will be used further to get necessary parameters by sampling the data. We can also generate what are known as corner plot to analyze individual correlations between any two unknown parameters.

5.2 Galaxy Rotation Curves: Revisited

A brightness spectrum, as we already saw before is the Brightness vs Wavelength (bandwidth) curve. And what we start with is the synthesized dataset containing the required data to obtain the H-21cm spectrum for each star in a certain galaxy, labeled with its distance from the observer (earth). And to finally plot a galaxy rotation curve of that galaxy, our task will be first to obtain the outward radial velocities of each star. This can be done once we get the redshifts of each star. And finally, the plot of radial velocities with respect to the distances gives us the final curve.

One trivial way of getting redshifts is to literally see how much the wavelength has shifted from the state of the emitted beam to the observed beam. The beam (spectrum) we are observing here is the Hydrogen 21cm line, whose sources of emissions are clearly identified meaning we can calculate the exact emission frequency (or wavelength) using quantum mechanics. This has been done already and it is known for the fact that the emission wavelength is 21.106 cm (or 1420.405 MHz in frequency terms). But for the sake of simplicity owing to the data generation process, we consider 21.0 cm as the emission wavelength for comparisons. Now we iteratively open each file, record its radial distance, and plots its spectrum curve. Most of the plots corresponded to a delta function-like distribution or an extremely squeezed Gaussian peaking at its observed frequency only as shown. The next task involves finding the central maxima of the peak by fitting a gaussian to this, we accomplish it this time using MCMC fitting. The end result of this fitting
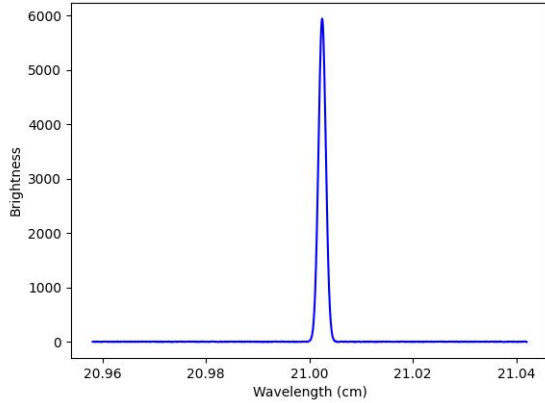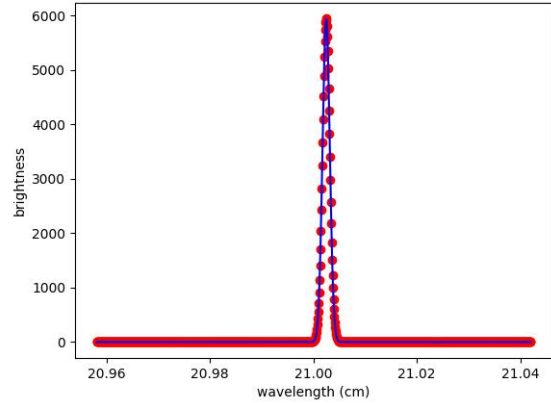
Figure 5.1: Continuous plot of data points

Figure 5.2: Data after fitting a Gaussian. Red points denote initial data points

Figure 5.3: Synthetic Spectrum for a star at radial distance 0.69 kpc

is the wavelength corresponding central peak of the spectrum. This wavelength does not (and should not) be equal to 21cm owing to the redshift caused by the relative velocity between the observer and the target. Our next step is to just record the wavelength and obtain the redshift using the following equation.

$$z = \frac{\lambda_{central} - \lambda_{21cm}}{\lambda_{21cm}}$$

Once we get the redshifts, radial velocities are obtained using this formula,

$$v = c \cdot \frac{(z+1)^2 - 1}{(z+1)^2 + 1}$$

Once done iterating through all the data entries, we can proceed with plotting the Radial velocity vs Radial Distance curve (or the Galaxy Rotation Curve). The final curve is shown in Fig 5.4, and it should be the same as the one in Fig 2.3 as the fit parameters, obtained either by MCMC or a regression fit has to converge to the same answer. And as expected, we find the same results.

One additional convenience provided by emcee's MCMC sampling over Scipy's curve fit is the ability to extract correlation plots or corner plots. The corner plots obtained are shown in Fig 5.5. The plots however did not show a clean correlation between any two parameters (explain further). The poorly explainable corner plots obtained might be due to the nature of the problem itself, where we are fitting gaussians to (almost) delta functions, with too high amplitudes and too low spreads.

5.3   Sampling Light Curve Parameters for GW170817

A smooth broken power law is a functional form used to model light curves in astronomy, particularly for objects that display a change in their emission behavior at a certain point in time. It consists of two power-law segments that are smoothly connected at a break point. The smoothness ensures a continuous transition
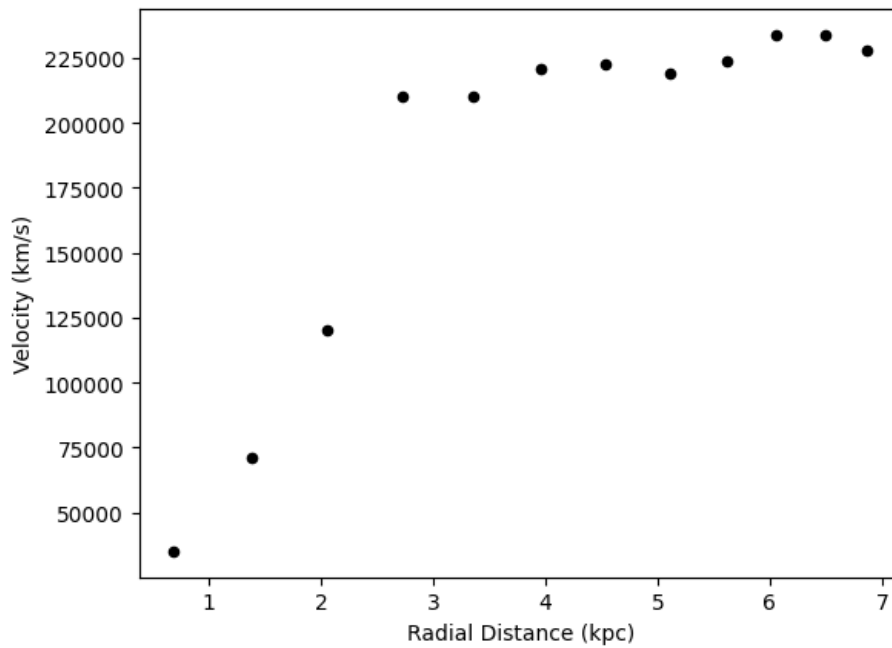
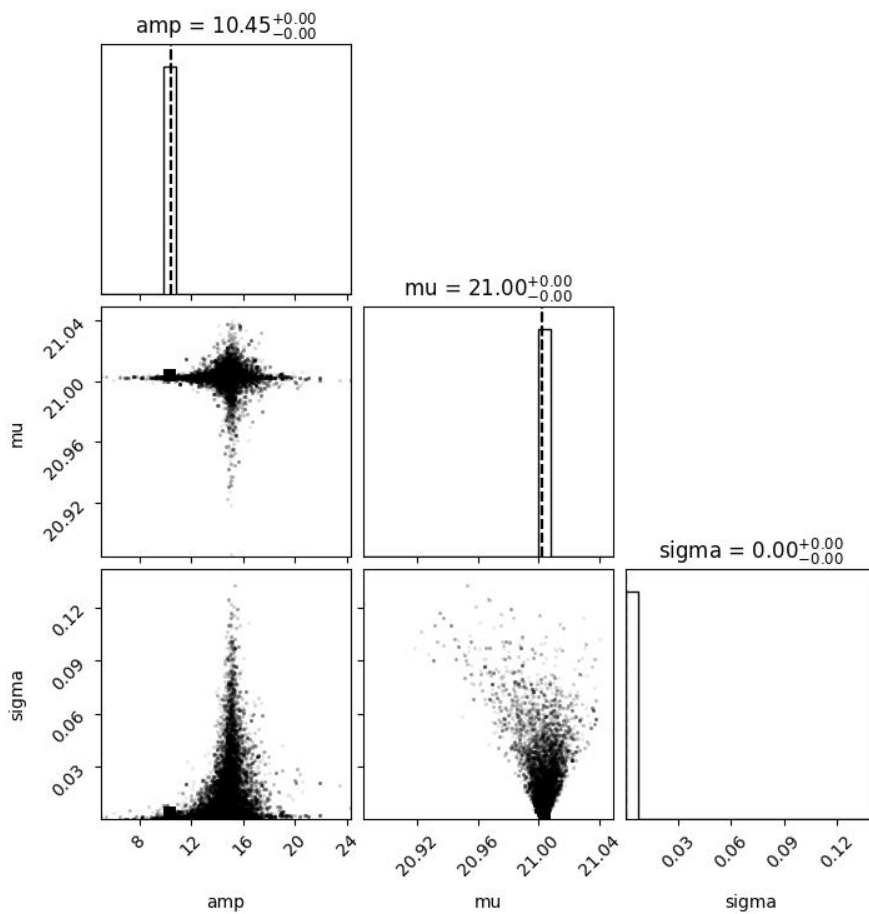Figure 5.4: Galaxy Rotation Curve plotted out of calculated redshifts of each source

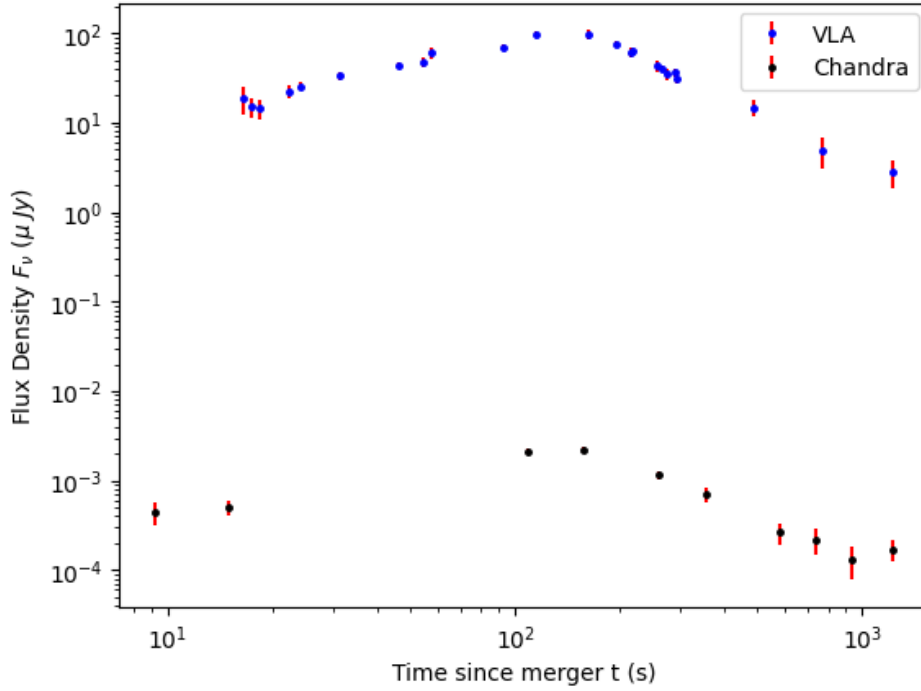Figure 5.5: Correlation Plots from fitting a Gaussian's to data of one source

Figure 5.6: GW170817 Light Curves from VLA and Chandra telescopes

between the two power laws, resulting in a more physically plausible representation of the light curve. The smooth broken power law can be expressed as follows:

$$F(t,\nu) = 2^{1/s} \cdot (\frac{\nu}{3GHz})^{\beta} \cdot F_p \left[(\frac{t}{t_p})^{-s\alpha_1} + \frac{t}{t_p}^{-s\alpha_2} \right]^{-1/s}$$

where: $F(t,\nu)$ is the flux or intensity of the light curve at time,
F_p is the peak flux,
t_p is the time at which light curve reaches its peak,
t is the time post merger,
ν is the observing frequency,
and rest of them ie, $\beta, \alpha_1, \alpha_2, and s$ are model specific parameters.

Now, the MCMC process involves creating a model light curve based on the smooth broken power law and computing the likelihood of the observed data given the model. The likelihood quantifies how well the model light curve matches the observed data, considering uncertainties in the data points. The MCMC algorithm samples the parameter space, proposing new sets of parameter values and accepting or rejecting them based on their likelihood compared to the current values. It explores regions of parameter space that have higher likelihood values, seeking the best-fit parameters that explain the observed light curve. As with the first activity, data from the VLA and Chandra telescopes are separated initially and then fed into the sampler. The lightcurves from VLA and Chandra telescopes are shown here.

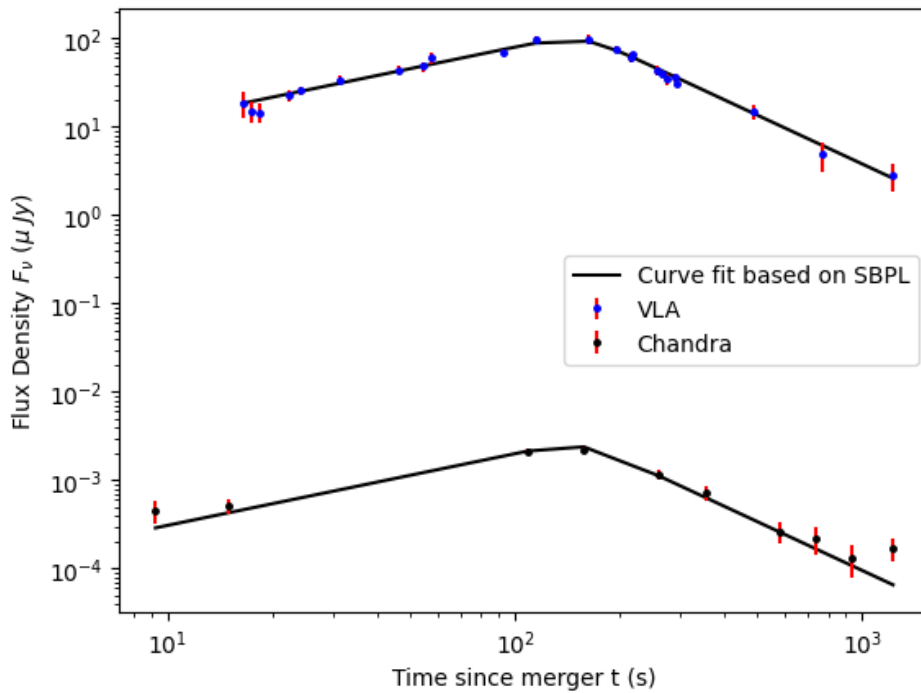With 6 parameters to be sampled in the smooth broken power law, we set up the

Figure 5.7: Plot after fitting Smooth Broken Power Law to the light curve

subroutines as described and start the sampling process. The curve of function constructed from the converged results, plotted against the initial data is displayed below.

Analysing the corner plots of this sampling, we find better plots from the last attempt, indicating a reasonably good fit for the model we started with. And circular regions show us that there is a visible smooth correlation between the parameters. The correlation plots are shown in Fig 5.8 for further reference.
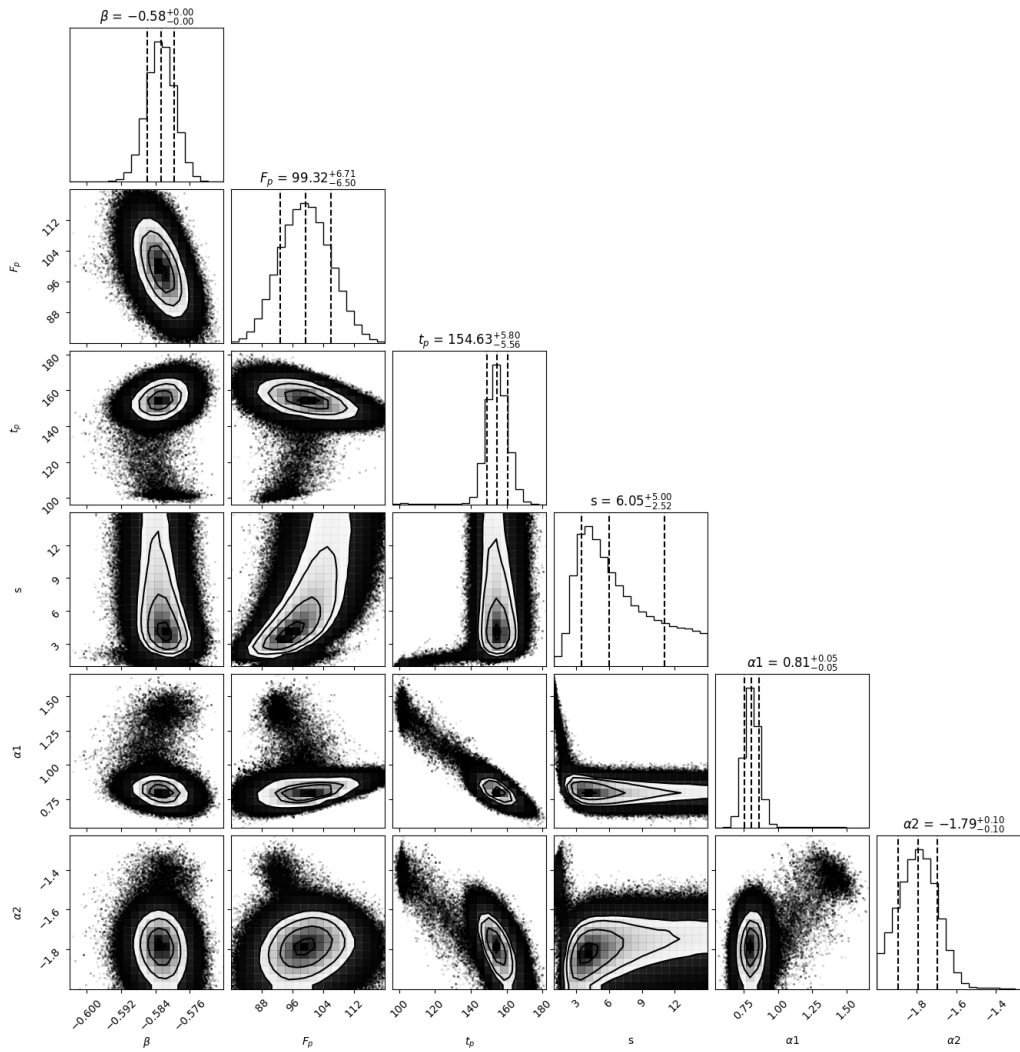
Figure 5.8: Correlation Plots of Fitting SBPL to GW170817 light curves
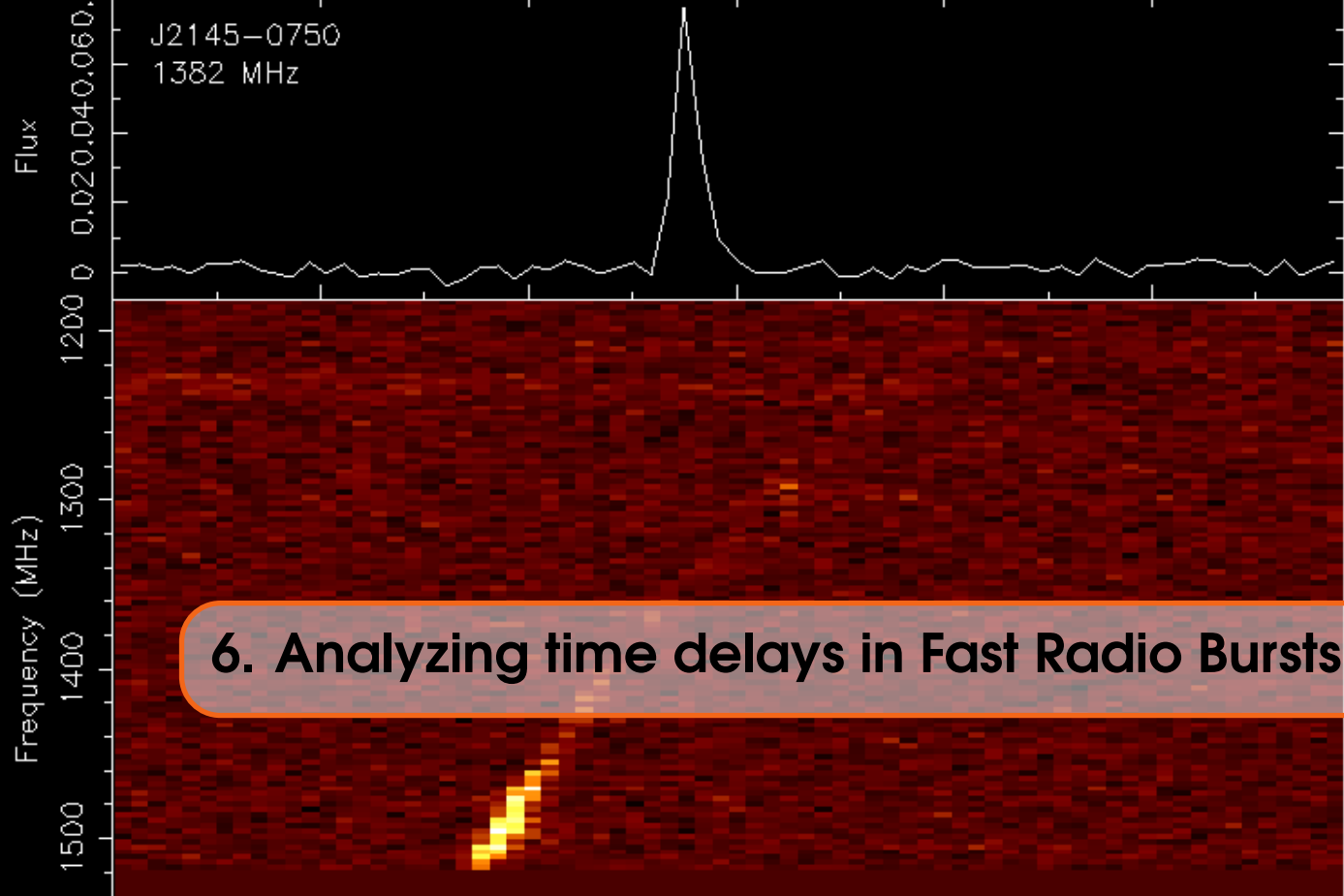
6. Analyzing time delays in Fast Radio Bursts

Fast Radio Bursts (FRBs) are intriguing and intense bursts of radio waves, lasting only a few milliseconds. These high-energy events have puzzled astronomers since their discovery, as their origins remain elusive. FRBs have been observed coming from various sources, including distant galaxies, making their study a challenging but crucial endeavor. Proposed explanations for FRBs include cataclysmic events like neutron star mergers, highly magnetized neutron stars known as magnetars, and even more speculative possibilities of undiscovered phenomena.

To observe FRBs, radio astronomers employ sensitive radio telescopes equipped with wide-field receivers. When an FRB event occurs, the telescope rapidly records the burst of radio waves. The transient nature of FRBs makes their detection and study particularly demanding, requiring sophisticated data processing techniques to pinpoint their exact locations and characteristics. Thanks to advancements in radio telescope technology, like the CHIME and ASKAP telescopes, the detection rate of FRBs has increased significantly in recent years. Studying these cosmic mysteries opens up a realm of possibilities to explore extreme astrophysical phenomena and gain new insights into the distant and energetic regions of the universe, and they are one of the active sites of astronomy research in recent times.

The signals from a pulsar or any FRB arrive at different times for different frequencies ie., signal gets more and more delayed as the frequency decreases. With the highest frequency signals arriving first. This phenomenon is caused by dispersion. Dispersion occurs due to the presence of free electrons along the line of sight between the source (FRB or pulsar) and the observer, typically as the radio waves travel through the interstellar medium of our galaxy or even the intergalactic medium for extragalactic sources.

6.1   Time delays due to dispersion and Corrections:

The dispersion effect arises because radio waves with higher frequencies (shorter wavelengths) travel slightly faster through the interstellar medium than radio waves with lower frequencies (longer wavelengths). The higher frequency waves experience less scattering and interaction with free electrons, leading to a shorter delay in their arrival time compared to the lower frequency waves, which are more strongly affected by dispersion.

As the radio waves from an FRB or a pulsar propagate through the interstellar medium, the delay due to dispersion accumulates with increasing wavelength. This dispersion delay can be quantified using the dispersion measure (DM), which is a measure of the total electron content along the line of sight. The DM is expressed in units of pc/cm³ (parsec per cubic centimeter) and provides crucial information about the density of free electrons in the interstellar medium.

Radio astronomers use sophisticated techniques to correct for dispersion effects when analyzing data from FRBs or pulsars. By applying dispersion corrections, they can align the different frequency channels to account for the dispersion delays, reconstructing the original, undispersed pulse shape or burst profile. These corrections are done using explicit time delays for each frequency band. These time delays are obtained using the equation,

$$T_{arr} = 4148.808 \cdot DM \cdot \nu^{-2}$$

6.1.1   Correction Process

The correction process we imply here is to first convert the signal's observation into an image, and with that conversion, the frequency (y-axis) and the time of arrival (x-axis) gets discretized into their respective bins. And then we explicitly calculate the time delays for each frequency bin and shift them appropriately until the peak lines up. This process is easy least how it is described, but the problem here lies with the parameter called DM (Dispersion Measure), which cannot be known theoretically beforehand, and requires a little trial and error to arrive at its correct estimate. This estimation of Dispersion measure constitutes this task, using the data from the burst of pulsar in recent times. It is also important to say similar procedure to estimate the DM, can also be applied to correct FRB's data.

Finally, rather than relying on our own perception of the 'peak lining up' as a vertical line, we use a quantitative measure of the same thing called the Signal to Noise Ratio (SNR) for this time series and aim to pick a DM that maximise it. Here we define our SNR to be ratio of maximum and mean values of the time series fluxes. The time series is gotten beforehand by summing over the flux densities over the range of frequencies at a particular time bin considered. By following this method, we can automate the peak lining up procedure and ensure a more accurate value of DM.

6.2   Dispersion Measure of Pulsar burst:

We start the analysis with a 2D numpy array representing the image of the signal obtained. The information on the Y-axis (Frequency) and X-axis (time) bins is also given. The Frequency ranges from 400 MHz to 800 MHz (with increasing y-axis) in 32 bins, and the Time periods fit in bins of 16ms each. A quick look at the 2D arrays shape reveal the image size being 32x254, and the time periods go until 4.048s
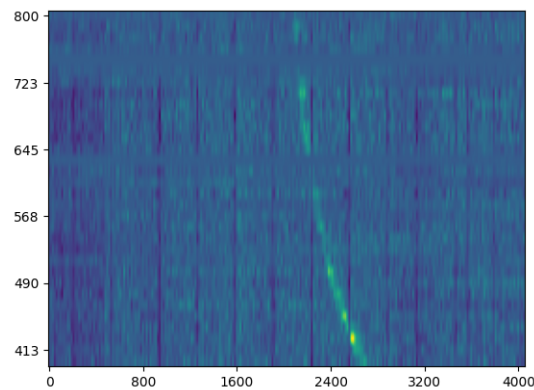
Figure 6.1: Image of the initial pulse data

from start to finish of the capture. Setting up required bins to label the data, the initial image of the pulse is shown in Fig 6.1, revealing the time delays for each frequency quite clearly.

Our next task should be to obtain the time differences for each frequency bin, which amounts to just choosing a suitable DM and evaluating the function n-times. Now comes the correction process, where we convert the time delay into the number of x-bins a row has to be shifted, and shift it. One thing to take care of while shifting is whether you are shifting the row of pixels right or left. Since the time delays are to be subtracted as we go down the y-axis rows, they have to be shifted right. Though it does not affect the DM we get in the end, this can become a mistake if further analyses are to be done with the corrected peak.

(a) DM = 1   (b) DM = 12   (c) DM = 25
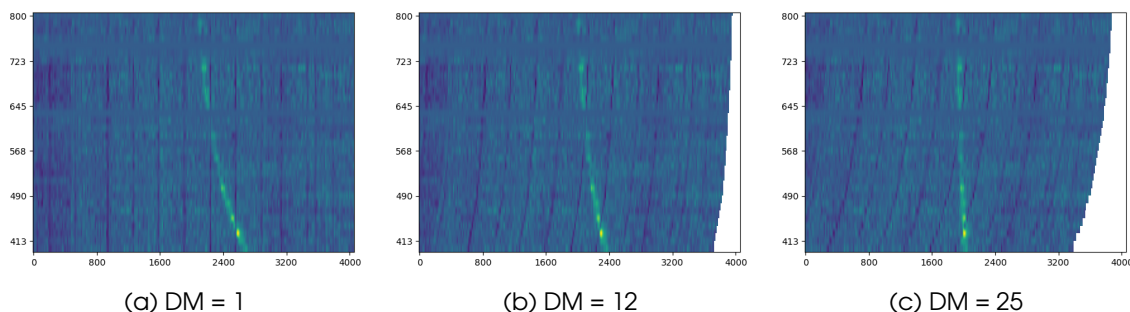
Figure 6.2: Progression of corrections with increasing values of DM.

The three images in Fig 6.2 from left to right above show how the peak gets corrected as we approach the right value of DM. And the image below shows the peak lined up perfectly for the DM of 30.25, for which we get the maximum SNR of around 16. We calculate SNRs for this image by considering a particular time bin, each pixel value as we know represents the flux density at that point. We the get the time series by summing over all frequencies at one time bin and consider their absolute values only. This is done to eliminate any effects of negative values on the SNR. Once we get the time series SNR is calculate by the ratio of maximum to mean of absolute time series.

Even though the maximum SNR is of little interest here, the DM for which we maximise the SNR dictates the result. The variation of SNR with respect to the DM is
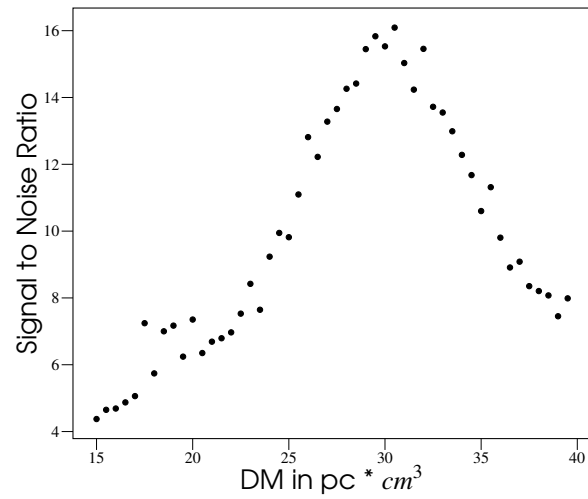
Figure 6.3: Variation of SNR with DM

also shown in Fig. 6.3 This clearly points out to the DM where the vertical peak is observed.

Refernces

Books

- Marr, J. M., Snell, R. L., amp; Kurtz, S. E. (2020). Fundamentals of Radio Astronomy: Observational Methods. CRC Press.

Images

- VLA Image - Radio astronomy. (2023, June 8). In Wikipedia.
  https://en.wikipedia.org/wiki/Radio_astronomy
- Black Hole Image - Event Horizon Telescope. (2023, June 19). In Wikipedia.
  https://en.wikipedia.org/wiki/Event_Horizon_Telescope
- MCMC Image - Tutorial on MCMC by Imad Pasha.
  https://prappleizer.github.io/Tutorials/MCMC/MCMC_Tutorial.html
- TW Hydra Image - Credits: NASA, ESA/Hubble. January 7, 2017 News Release.
  https://hubblesite.org/contents/news-releases/2017/news-2017-03.html
- Peryton Event (FRB Chapter Image) - Psr1909, CC BY-SA 4.0
  https://creativecommons.org/licenses/by-sa/4.0, via Wikimedia Commons

Code Repository

- Github Repository of Python jupyter notebooks at
  https://github.com/NV-Karthik/radio-astronomy-techniques

Index

S

T